A Reduced Order Modeling Approach to Blunt-Body Aerodynamic Modeling

Hayden V. Dean*, Kenneth Decker †, Bradford E. Robertson‡, and Dimitri N. Mavris§
Aerospace Systems Design Laboratory, Georgia Institute of Technology, Atlanta, GA, 30332

Blunt-body entry vehicles display complex flow phenomena that results in dynamic instabilities in the low supersonic to transonic flight regime. Dynamic stability coefficients are typically calculated through parameter identification and trajectory regression techniques using both physical test data and Computational Fluid Dynamics (CFD) simulations. This methodology can generate dynamic stability coefficients, but the resulting data points are limited, and have high degrees of uncertainty due to the nature of data reduction methods. With increased computational capabilities, new methods for dynamic stability quantification have been explored that seek to leverage the high-dimensional aerodynamic data produced from CFD simulations to compute dynamic stability behavior and address the limitations of linearized aerodynamics. The objective of this work is to advance the quantification of dynamic stability behavior of blunt-body entry vehicles by leveraging high-fidelity CFD data through Reduced Order Modeling (ROM). ROMs are capable of leveraging high-fidelity aerodynamic data in a cost effective manner by finding a low-dimensional representation of the Full Order Model (FOM). ROMs based on Proper Orthogonal Decomposition (POD) have shown success in recreating CFD analyses of parametric ROM applications and time-varying ROM applications. Results of this research demonstrated success in constructing two ROMs of a notional blunt-body entry vehicle to recreate heatshield and backshell pressure distributions from forced oscillation trajectories. The ROM was more successful at reconstructing the heatshield pressure distribution, with challenges arising in predicting the chaotic response of backshell latent coordinates.

I. Nomenclature

A	=	Amplitude of the forcing function
A_i	=	Batch set of the snapshot matrix
C_{F_x}	=	Force Coefficient in the x-direction
C_{F_y}	=	Force Coefficient in the y-direction
C_{F_z}	=	Force Coefficient in the z-direction
C_{M_x}	=	Moment Coefficient in the x-direction
C_{M_y}	=	Moment Coefficient in the y-direction
C_{M_z}	=	Moment Coefficient in the z-direction
C_P	=	Coefficient of Pressure
d	=	ROM dimension
f	=	Generic function operator
f^*	=	Dimensional frequency of forcing function
ff	=	Forget Factor of Streaming Singular Value Decomposition
g	=	Regression function operator
i, j	=	Generic indices
k	=	preserved left singular vectors
M_∞	=	Mach number
m	=	Number of snapshots

*Graduate Researcher, ASDL, School of Aerospace Engineering, Georgia Tech, AIAA Student Member
†Research Engineer II, ASDL, School of Aerospace Engineering, Georgia Tech, AIAA Member
‡Research Engineer II, ASDL, School of Aerospace Engineering, Georgia Tech, AIAA Member
§S.P. Langley Distinguished Regents Professor and Director of ASDL, Georgia Tech, AIAA Fellow

n	=	Degrees of Freedom of samples
$\mathbf{p}$	=	Vector of design variables
r	=	Covariance matrix rank
$\mathbf{S}$	=	Data Covariance Matrix
t^*	=	Dimensional time
v	=	Number of validation snapshots
$\mathbf{X}$	=	Matrix of snapshots
$\mathbf{x}$	=	Single snapshot
$\mathbf{Z}$	=	Matrix of latent coordinates
$\mathbf{z}$	=	Single latent coordinate
α	=	Angle of Attack
$\dot{\alpha}$	=	Rate of Change of Angle of Attack
δ	=	Desired information content
μ	=	Average of the Input Snapshot Matrix
σ	=	Singular value
$\mathbf{\Phi}$	=	POD Mode Matrix
ϕ	=	POD mode
ANN	=	Artificial Neural Network
ASDL	=	Aerospace Systems Design Laboratory
CFD	=	Computational Fluid Dynamics
DOF	=	Degrees-of-Freedom
DR	=	Dimensionality Reduction
EDL	=	Entry, Descent, and Landing
FF-CFD	=	Free-Flight Computational Fluid Dynamics
FOM	=	Full-Order Model
FUN3D	=	Fully-Unstructured Navier-Stokes 3D
MAE	=	Mean Absolute Error
PCA	=	Principal Component Analysis
POD	=	Proper Orthogonal Decomposition
RBD	=	Rigid Body Dynamics
RBF	=	Radial Basis Function
RIC	=	Relative Information Content
SIAD	=	Supersonic Inflatable Aerodynamic Decelerator
SVD	=	Singular Value Decomposition

II. Introduction

Entry, descent, and landing (EDL) is critical to successful planetary missions. EDL vehicles must be able to withstand the stresses of entry, sufficiently slow down, and preserve the integrity of the landed payload. For decades, the solution has been the blunt-body entry vehicle, which is capable of generating the large amounts of drag necessary for atmospheric entry, and dissipating the heat of entry over a large area. The heatshield shape is selected based on heating and stability constraints [1], whereas the backshell shape is selected based on packaging and mass requirements of the vehicle payload.

Blunt-body entry vehicles can be dynamically unstable in the supersonic to transonic flight regimes, becoming more unstable as the vehicle decelerates [1]. This is a well-documented, and undesired behavior resulting from unsteady recirculating wake combined with deceleration and oscillations of the vehicle [2]. Understanding the physical phenomena that drives blunt-body dynamic instability is a major research effort [3–6]. Physical tests, the accepted way to quantify dynamic stability of blunt-body entry vehicles, range from forced oscillation tests, free-oscillation tests, free-flight wind tunnel tests, and ballistic range tests [1, 7–10]. In addition to flight testing, Computational Fluid Dynamics (CFD) simulations are a growing area of research in dynamic stability quantification, often used to supplement dynamic stability data [4, 7, 11–17]. Deciphering dynamic stability coefficients from testing methods is a complex task. Linear and quasi-static assumptions are made, and a functional form is utilized to determine dynamic stability coefficients via trajectory-fitting techniques [1]. Assuming the dynamic behavior of the capsule is linear and quasi-static may be flawed, as literature has noted the nonlinear dynamic nature of these vehicles [7]. Therefore, there is a need to develop new methodologies to quantify the dynamic behavior of entry capsules.

Research efforts in dynamic stability quantification have been focused on finding innovative ways to quantify blunt-body dynamic stability, moving away from traditional, linearized functional forms. McKown et al. (2022) used 1-degree-of-freedom (1DOF) Free-Flight CFD (FF-CFD) to generate vehicle trajectories of the Genesis entry capsule to investigate the use of non-linear pitch damping coefficient curves [18]. Results showed improved performance on predicting vehicle dynamic stability coefficients using inverse estimation methods [18]. Ernst et al. (2023) used feed-forward and time-delay neural networks to predict dynamic stability coefficients of a Supersonic Inflatable Aerodynamic Decelerator (SIAD) using data generated by a CFD-rigid body dynamics (RBD) modeling framework [13]. The neural networks outperformed the traditional limit cycle analysis outlined in [1] when used to predict aerodynamic coefficients [13], indicating the benefit of a lack of functional form.

Analytical functional forms limit model accuracy and expressiveness by assuming the vehicle response can be isolated to a coefficient response from a data fit surrogate model. It is possible that the dynamic response of entry capsules cannot be isolated to coefficients; thus, developing advanced functional forms won't be enough. Existing data reduction techniques omit the rich data that can be obtained from CFD simulations. This aerodynamic information could be critical to discovering new methods for dynamic stability quantification. To avoid traditional data fit methods and discover new methods for expressing the dynamic response of entry capsules, the rich data produced from CFD simulations should be leveraged.

Reduced Order Modeling (ROM) is a form of surrogate modeling with the ability to leverage high-fidelity aerodynamic data in a computational efficient manner [19–25]. In a single model, a ROM can produce a field of responses, mimicking the results produced by CFD simulations [25]. ROMs handle the size and complexity of aerodynamic data by finding a low-dimensional representation of the data called the *latent space* that captures fundamental features of the original high-dimensional data [19, 26]. This latent space can be leveraged to make predictions of the high-dimensional field at unseen parameter points [19]. In general, ROMs are classified in one of two ways: intrusive, and non-intrusive [19, 27]. Intrusive ROMs are provided the governing equations used to generate the Full Order Model (FOM), often requiring modifications to source code to enable their use [28–31]. Non-intrusive ROMs are a data-driven method that only require the input and output data for training, a favorable characteristic in aerospace applications that often leverage "black box" analysis codes [19, 32].

ROMs have been applied to numerous applications similar to the blunt-body entry vehicle problem, including vortex shedding behind a rotating cylinder [33], turbulent flows [34], axisymmetric turbulent wake behind a disk [35], parametric applications in compressible flow [20], and unsteady aerodynamics [36]. ROM literature primarily focuses on modeling two types of fluid flows: parametrically varying fluid flows, and time-varying fluid flows. Parametrically varying ROMs focus on the parametric prediction of steady flow fields, most commonly varying Mach and angle of attack (α) [27]. Examples of Parametric ROMs include airfoils at different Mach and α configurations [19, 20, 22, 37–40], hypersonic aerodynamics [23] and rotorcraft aerodynamics [41]. Time-varying ROMs focus on decomposing unsteady fluid flows, focusing on modal decomposition and identifying dominant structures in the flow. Examples of time-varying ROMs include cylinder wakes [33, 42–44], aeroelastic analysis [45], and wind turbine analysis [46, 47]. Literature combining parametric and time-varying ROMs, a critical capability when developing a entry vehicle ROM to predict the dynamic response of the vehicle at different vehicle states, is an emerging area of research. Constructing a parametric and time-varying ROM of an entry capsule will enable the dynamic prediction of aerodynamic fields, providing time-accurate predictions of the vehicle response in a computationally efficient manner. Applications of parametric ROMs and time-varying ROMs have leveraged Principal Component Analysis (PCA), also called Proper Orthogonal Decomposition (POD). POD is a linear Dimensionality Reduction (DR) technique that uses eigenvalue decomposition to determine the dominant features present in the data [48]. POD is capable of deciphering spatial structures present in the FOM when leveraged in parametric ROMs, and is capable of deciphering temporal structures of a FOM when applied in time-varying ROMs [44].

The objective of this research is to advance the ability to quantify dynamic stability of blunt-body entry vehicles by leveraging high-fidelity CFD data using a parametrically time-varying POD ROM. The remainder of this paper is organized into six sections. The third section outlines more specifics on the ROM methodology begin applied in this research. The fourth section describes the application being tested to demonstrate this methodology. The fifth section shows the results of the research. The sixth section summarizes the conclusion and lists future work in this research area.

III. Reduced Order Modeling Methodology

This section outlines the ROM methodology and necessary mathematical formulations of developing a parametrically time-varying POD ROM of an entry capsule. A ROM can be divided into 4 main parts: training data generation, DR, interpolation or regression, and back-mapping. Each part of the ROM will be summarized below, outlining any necessary mathematical formulations for implementation.

A. Training Data Generation

The first step is to identify the input state space to be represented by the ROM. CFD simulation enables the sampling of pressure and shear distributions across the vehicle as a result of the flow field. Previous studies have demonstrated ROM's abilities to capture and predict flow features in blunt-body wakes [20, 33–35, 49]. The off-body flow features contain complex structures, including shocks and expansions in the supersonic flow regime, that can be difficult for ROMs to capture and may require significantly more training samples to resolve the underlying behavior to an appropriate level of accuracy [19]. The outer flow field (e.g. wake, and far-wake flow field) leaves a footprint of the complex interactions on the vehicle surface, impacting the resulting surface pressure and shear distributions. These distributions ultimately produce the forces and moments that drive the vehicle dynamics. Therefore, if the pressure and shear distributions on the vehicle's surface can be generated by the ROM, then the time-accurate vehicle dynamics can be predicted. Initially, this research will focus on developing a ROM capable of predicting surface pressure distributions for an entry capsule. The synthesized methodology will be equally applicable for reconstructing surface shear distributions in future work.

Next, the parameters of the vehicle input state space need to be identified, establishing the upper and lower bounds that need to be sampled. This research will focus on an entry capsule input space with a constant Mach number, varying in angle of attack, α, and rate of change of angle of attack, $\dot{\alpha}$. This input space will be generated by sampling forced oscillation CFD simulations. Forced oscillation is a dynamic testing technique where the vehicle is "forced" through prescribed oscillatory motions, most commonly by simulated sinusoidal motion [1, 50]. The forced oscillation motion will be simulated using Fully Unstructured Navier-Stokes 3D (FUN3D), a CFD solver developed by NASA Langley Research Center [51]. In FUN3D, the vehicle motion in forced oscillation is controlled by:

$$\alpha(t) = A\sin(2\pi f^* t^*) \tag{1}$$

the resulting $\dot{\alpha}$ is given by integrating Equation 1:

$$\dot{\alpha}(t) = 2\pi f^* A\cos(2\pi f^* t^*) \tag{2}$$

where A is the amplitude of oscillation, f^* is the dimensional frequency of oscillation, and t^* is the dimensional time. Through combinations of A and f^*, a series of trajectories can be simulated spanning an $[\alpha, \dot{\alpha}]$ state space of the entry vehicle. Each sampled time step in a CFD simulation provides a single snapshot for the input matrix of the ROM. Therefore, a single forced oscillation trajectory can provide thousands of parametrically time-varying snapshots for the ROM to train with.

B. Dimensionality Reduction

After generating the training set of data, a DR technique must be selected to construct the low-dimensional space of the ROM. DR is a form of unsupervised machine learning where high-dimensional data is projected into the latent space that preserves some quality of the original data [19]. POD, also referred to as Principal Component Analysis (PCA) or Karhunen-Loève Decomposition, is the most commonly applied DR technique in literature [48]. POD was first introduced as a mathematical technique to extract structures present in turbulent fluid flows [48]. An objective algorithm in POD decomposes the FOM into a minimal number of *modes*, or basis functions, that capture the highest amount of energy of the FOM [48]. This research will implement a non-intrusive, or data-driven, variant of POD called *snapshot POD*. The original derivation of POD by Berkooz et al. can be found in [34].

From the sampled forced oscillation simulations, an input snapshot matrix $\mathbf{X}$ is generated with m snapshots and n degrees of freedom of the response variable of interest. In this entry vehicle ROM, m represents the number of samples of the CFD simulation, and n represents the number of degrees of freedom of the pressure data. For this application, the pressure data is being calculated at discretized points associated with the CFD grid. Depending on the sampled CFD solver, the CFD grid can produce pressure data associated with grid cells or grid nodes. The n dimension of the input snapshot matrix quickly becomes large in entry vehicle applications due to CFD grid sizes. FUN3D is a node-based CFD solver [51]; therefore in this application, n represents the number of nodes on the vehicle surface, with each node producing a C_P value to be predicted by the ROM. The result of the CFD simulations is $\mathbf{X} = [\mathbf{x}^1, ..., \mathbf{x}^m] \in \mathbb{R}^{nxm}$. Before applying POD, $\mathbf{X}$ is mean centered, resulting in [19]:

$$\bar{\mathbf{x}} = \frac{1}{m}\sum_{j}^{m} \mathbf{x}_j = 0 \tag{3}$$

POD projects the high-dimensional snapshot matrix $\mathbf{X}$ into the low-dimensional latent space spanned by orthonormal basis vectors called *modes* [19]. The columns of the mode matrix, $\mathbf{\Phi}$, consist of a set of orthonormal modes, $\mathbf{\Phi} = [\boldsymbol{\phi}^1, ..., \boldsymbol{\phi}^d] \in \mathbb{R}^{nxd}$, where d defines the dimension of the latent space and number of preserved modes [19]. By optimizing the Rayleigh quotient [52]:

$$max_{\boldsymbol{\phi_j}} \frac{\boldsymbol{\phi_j^T S \phi_j}}{\boldsymbol{\phi_j^T \phi_j}} \tag{4}$$

the number of preserved POD modes can be determined, where $\boldsymbol{S} = \frac{1}{m}\boldsymbol{X}\boldsymbol{X^T}$ is a sample data covariance matrix [19]. The mode matrix $\mathbf{\Phi}$ is calculated by performing Singular Value Decomposition (SVD) on the input snapshot matrix $\boldsymbol{X}$ [19]:

$$\boldsymbol{X} = \boldsymbol{U\Sigma V^T} \tag{5}$$

where $\boldsymbol{U} \in \mathbb{R}^{nxn}$, $\boldsymbol{V} \in \mathbb{R}^{mxm}$, and $\mathbf{\Sigma} = diag(\sigma_1, ..., \sigma_r) \in \mathbb{R}^{nxm}$ such that $\sigma_1 \geq \sigma_2 \geq ... \geq \sigma_r \geq 0$ and $r = min(n, m)$ [19, 31]. The eigenvectors of $\frac{1}{m}\boldsymbol{X^T X}$ are the columns of $\boldsymbol{V}$, and the eigenvectors of $\frac{1}{m}\boldsymbol{X X^T}$ are the columns $\boldsymbol{U}$, with corresponding eigenvalues defined by $\sigma_1^2, ..., \sigma_p^2$ [19].

The main challenge in POD is that SVD can be computationally expensive with large matrices. Traditional SVD methods result in computation scaling with $O(nm^2)$, requiring $O(nm)$ of memory [53]. Recall in this entry capsule problem, n represents the number of nodes on the surface of the vehicle, and m represents the number of snapshots or CFD samples. To improve the computationally efficiency of the SVD component in POD, a streaming SVD algorithm developed by Maulik and Mengaldo (2021) [53] was implemented. Instead of performing SVD on the full input matrix $\mathbf{X}$, a QR-decomposition is applied to a batch set of data, A_i, and then SVD is applied to the resulting upper triangle matrix, R [53]. Additionally, the user specifies a value k to define the amount of preserved left singular vectors or largest coherent structures to preserve, and a forget factor, $ff \in [0, 1]$, to control the effect of older batches on the final result of the streaming SVD [53]. For specifics on the streaming SVD algorithm, see references [53, 54]. In this application, $ff = 1.0$ so that the SVD utilizes all the batches equally [53]. Due to the significant number of unsteady time steps being sampled to construct this ROM, a value k is selected where $k << m$ and $k > d$ to preserve as much variance as possible in each batch before optimizing the number of preserved POD modes. The streaming SVD method reduces the computation cost of SVD to $O(nmk)$ operations and $O(nk)$ of memory, enabling the rapid eigenvalue decomposition of the entry capsule input snapshot matrix [53].

The columns of $\boldsymbol{U}$ represent the POD modes, $\boldsymbol{\phi}_j$ [19]. A low-rank matrix $\boldsymbol{U'} \in \mathbb{R}^{nxd}$ can be obtained by determining a rank d where $d < r$ [52]. This is achieved by arranging the $\mathbf{\Sigma}$ and the corresponding columns of $\boldsymbol{U}$ in descending order, then preserving the first d columns of $\boldsymbol{U}$ that correspond to the largest singular values in $\mathbf{\Sigma}$ [19]. The Relative Information Content (RIC) of including d basis vectors in a reduced rank model is defined as [19, 52]:

$$RIC(d) = \frac{\sum_{i=1}^{d} \sigma_i^2}{\sum_{j=1}^{r} \sigma_j^2} \tag{6}$$

The number of basis vectors d to be preserved in a POD approximation must be specified by the user [19]. The desired information content $\delta \in [0, 1]$ is selected, resulting in the preservation of d basis vectors that achieve $RIC(d) \geq \delta$ [19, 31]. In literature, values of $\delta \geq 0.99$ are commonly seen [19, 40]. After selecting the number of preserved modes, the latent space coordinates can be calculated by $\boldsymbol{Z = \Phi^T X}$, where the matrix $\boldsymbol{Z} = [z^1, ..., z^m] \in \mathbb{R}^{dxm}$ [19]. The latent space matrix $\boldsymbol{Z}$ can become increasingly large as thousands of m snapshots are provided by forced oscillation CFD simulations, regardless of the amount of POD modes identified by DR.

C. Interpolation or Regression

After the latent space matrix $\boldsymbol{Z}$ is generated, a parametric mapping is generated that can be used to predict unsampled latent space coordinates [19]. Interpolation or regression functions, g_i, are trained using input state space variables, $\boldsymbol{p}$ to predict coordinates in the latent space $\boldsymbol{z_i}$, resulting in $g_i : \boldsymbol{p} \mapsto \boldsymbol{z_i}$ [19]. With this research, the input state space, $\boldsymbol{p}$, is composed of α and $\dot{\alpha}$ pairings. These pairings are mapped to the generated latent space coordinates, allowing for the parametric prediction of unsampled latent space coordinates. A variety of interpolation and regression models have been used in ROM literature, including cubic splines [20], Radial Basis Functions (RBFs) [23, 40], Kriging [19], and Artificial Neural Networks (ANNs) [55]. In this research, a Kriging regressor with a Mátern 3/2 kernel optimized with a maximum log-likelihood criterion was leveraged to predict unseen latent coordinates [56].

D. Back-mapping

Leveraging the regression to predict an unsampled design point, $\boldsymbol{p}^*$, the predicted latent space coordinates can be transformed into the FOM through *back-mapping* techniques. By implementing POD as the DR technique, back-mapping is achieved by the linear projection $\boldsymbol{x}(\boldsymbol{p}^*) = \boldsymbol{\Phi z(p^*)}$ [19]. This relationship makes POD a favorable DR method, as there is a direct linear relationship between the latent coordinates and the full order space [19]. The resulting ROM from the established mathematical formulations is of the form shown in Equation 7. This equation summarizes the linear relationship between POD modes and the overall response of the ROM.

$$\hat{\boldsymbol{f}}(\boldsymbol{x};\boldsymbol{p}) = \boldsymbol{\mu}(\boldsymbol{x}) + \sum_{i=1}^{d} z_i(\boldsymbol{p})\boldsymbol{\phi}_i(\boldsymbol{x}) = \boldsymbol{\mu} + \boldsymbol{\Phi z} \tag{7}$$

E. Evaluating the ROM Performance

To evaluate the accuracy of the ROM, a validation forced oscillation trajectory is generated, resulting in v validation points. The predictive accuracy of the ROM is evaluated across the the validation trajectory using a series of quantitative and qualitative metrics. The total Mean Absolute Error (MAE) is used to assess the accuracy of the ROM at predicting the entire field and is calculated using:

$$MAE_{total} = \frac{\sum_{j=1}^{v} |\boldsymbol{x_j(p^*) - x_j^*}|}{v} \tag{8}$$

where $\boldsymbol{x}_j(\boldsymbol{p}^*)$ is the predicted field at the unsampled vehicle state, and $\boldsymbol{x}_j$ is the actual field at the unsampled point. The main sources of error in the ROM can be decomposed into two main sources: compression error and regression error. The compression error measures the error that is incurred when a FOM solution is projected into the ROM subspace, which can be computed using:

$$MAE_{comp} = \frac{\sum_{j=1}^{v} |\boldsymbol{\Phi\Phi^T x_j^* - x_j}|}{v} \tag{9}$$

where $\boldsymbol{\Phi\Phi^T x}_j^*$ is the reconstructed field using the POD modes, and $\boldsymbol{x}_j$ is the original field from the FOM. The regression error measures the accuracy with which the regression is able to predict the latent space coordinates at unseen points, and is generated using:

$$MAE_{reg} = \frac{\sum_{j=1}^{v} |\boldsymbol{z_j(p^*) - z_j}|}{v} \tag{10}$$

where $\boldsymbol{z}_j(\boldsymbol{p}^*)$ is the predicted latent coordinates an unsampled vehicle state, and $\boldsymbol{z}_j$ is the actual latent coordinates of the unsampled vehicle state. By splitting up the error between compression and regression, the ROM can be evaluated in a modular manner to assess the accuracy of each process.

Additionally, aerodynamic coefficients C_{F_x}, C_{F_y}, C_{F_z}, C_{M_x}, C_{M_y}, and C_{M_z} can be calculated by integrating the predicted ROM pressure field and comparing the results to the aerodynamic coefficients generated by FUN3D. Due to the forced pitching motion of the entry capsule, only C_{F_x}, C_{F_z}, and C_{M_y} will result in coherent trends. The other coefficients will only be a function of the chaotic nature of the wake; therefore, they will not be reported. Additionally, the predicted flow field and actual flow fields can be compared visually and analytically to demonstrate the effectiveness of the ROM to generate the unsampled flow field.

IV. Application: Genesis Sample Return Capsule (SRC)

To achieve the objective of this research of advancing the ability to quantify dynamic stability of blunt-body entry vehicle, an application or test case needs to be identified. This research will use the Genesis Sample Return Capsule (SRC) to construct a ROM using the methodology outlined in the previous section. Figure 1 shows a breakdown of the

Genesis SRC. Ballistic range testing identified dynamic instabilities, including a tumbling risk of the vehicle during longer flights [57]. Using the Genesis SRC as a test case for the ROM allows the results to be compared to ballistic range results, and compared to other ongoing studies on the Genesis SRC.

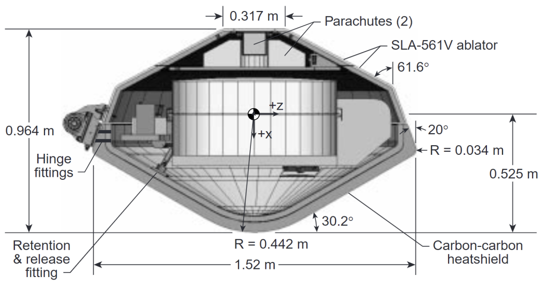

Fig. 1 Genesis Entry Vehicle [58]

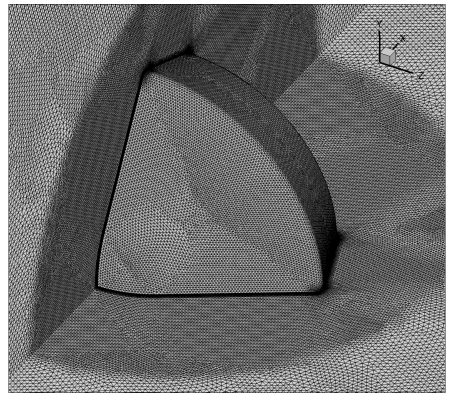

Fig. 2 Genesis Quarter Grid [59]

The CFD data for this ROM was generated by Willier et al. using an outer mold line provided by the NASA Langley Research Center [59]. The CFD grid totaled 53.8 million tetrahedral nodes [59]. More details about grid refinement and grid structure can be found in [59]. This grid results in 103,856 nodes on the vehicle surface used to track pressure data. Figure 3 shows the forced oscillation input state space sampled in this research. Table 1 summarizes the amplitude and frequencies used to generate the input space. Each forced oscillation CFD simulation was simulated at $M_\infty = 1.5$ and run for 20,000 time steps with $\Delta t^* = 582.9$ ns between each snapshot, resulting in 4 periods of oscillation. The first 5,000 time steps, 1 period of oscillation, of each sampled trajectory were removed from the data set to eliminate transients present in the CFD solution. A grand total of 240,000 snapshots of surface pressure data were generated from the forced oscillation CFD simulations.

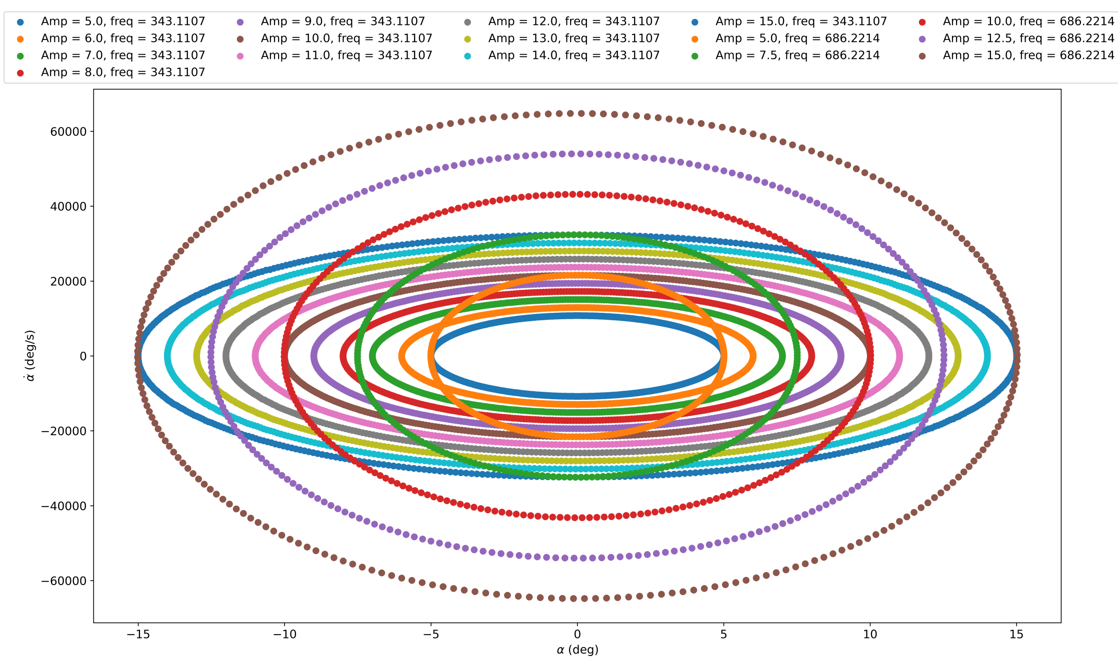

Fig. 3 Input State Space of Sampled forced oscillation CFD Simulations

Two ROMs were generated: a heatshield ROM, and a backshell ROM. Splitting the data aids in reducing the

Table 1 Summary of forced oscillation CFD Simulation Settings

Frequency, f^* (Hz)	Amplitude, A (deg)	Classification
343.11	5	Training
	6	Training
	7	Training
	8	Training
	9	Training
	10	Validation
	11	Training
	12	Training
	13	Training
	14	Training
	15	Training
686.22	5	Training
	7.5	Training
	10	Training
	12.5	Training
	15	Training

dimensionality of each ROM, and isolates the contribution of the heatshield and backshell pressure fields on the overall vehicle aerodynamic response. The same ROM methodology was applied to the heatshield and the backshell, the only difference being the RIC used for each ROM. Each input snapshot matrix was composed of CFD data from every 10^{th} CFD time step. The data provided by the $A = 10°$, $f^* = 343.11Hz$ forced oscillation trajectory was used as a validation data set, and was not included in the input snapshot matrices. The resulting snapshot matrix dimensions are summarized in Table 2.

Table 2 ROM Snapshot Matrix Dimensions

Component	Grid Nodes (n)	Snapshots (m)
Heatshield	39,988	22,500
Backshell	63,868	22,500

V. Results

Figure 4 shows the RIC plot for the constructed POD ROMs of the Genesis SRC heatshield and backshell. This plot indicates the variance is stored in each mode, and the necessary number of modes to achieve the specified RIC. Figure 4(a) shows that 10 modes are required to achieve an $RIC \geq 0.999$. Figure 4(b) shows that 46 modes are required to achieve an $RIC \geq 0.99$. A lower RIC was selected for the backshell ROM to minimize the computational requirements of training the regression on the backshell latent space. A significant amount of compression can be achieved using POD with streaming SVD. The MAE for the compression step was calculated using Equation 9. The true mean across all the heatshield nodes is 0.7535, with the MAE at each node ±0.0018 C_P units. The true mean across all the backshell nodes is −0.3064, with the MAE at each node ±0.0012 C_P units. These metrics are summarized in Table 3.

Figure 5 show a visualization of the first three POD modes on the heatshield of the vehicle. In total, there are 10 modes being utilized to reconstruct the FOM of the heatshield. The modes are linearly combined through inverse transformation relationships to build the FOM. POD modes are orthogonal allowing a ranking to be obtained by the modes according to how much variance is capture in each mode. Therefore, the first three modes shown below are the modes displaying the highest amount of variance in the model. Visualizing the POD modes provides an understanding

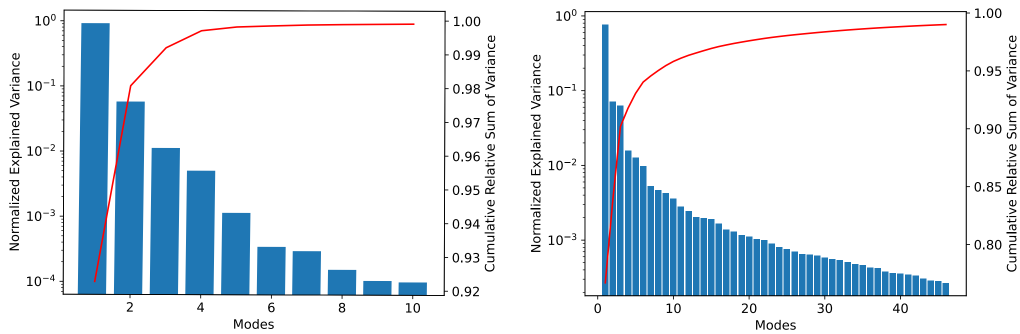

(a) Heatshield, $RIC \geq 0.999$ (b) Backshell, $RIC \geq 0.99$

Fig. 4 RIC Plot for Pressure ROM

of what behaviors the ROM is capturing in the data set. Figure 6 show a visualization of the first three POD modes on the backshell of the vehicle. In total, 46 modes are linearly combined to reconstruct the backshell pressure fields POD modes represent the dominate structures in the data that were recovered through DR. While literature notes that POD modes can represent non-physical features [44], these modes could provide insight into the root-cause of the dynamic response of entry capsules.

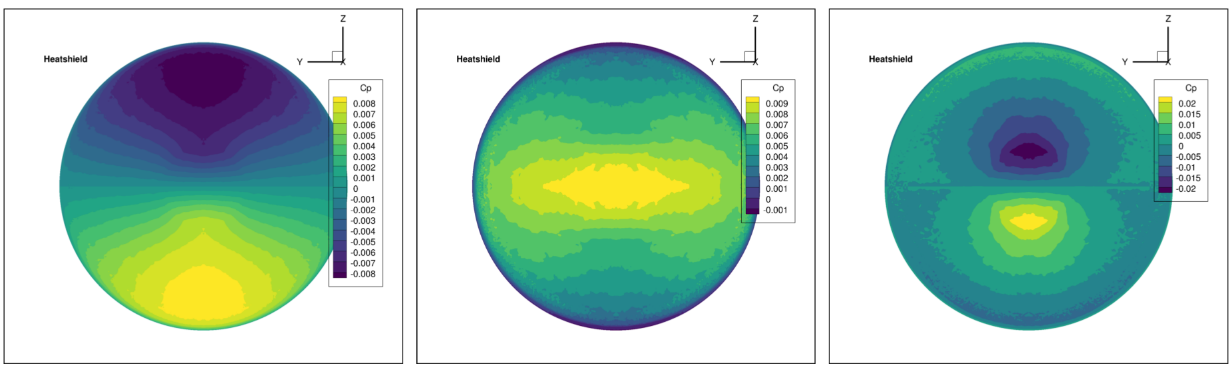

(a) Mode 1 (b) Mode 2 (c) Mode 3

Fig. 5 First 3 POD Modes for Heatshield ROM

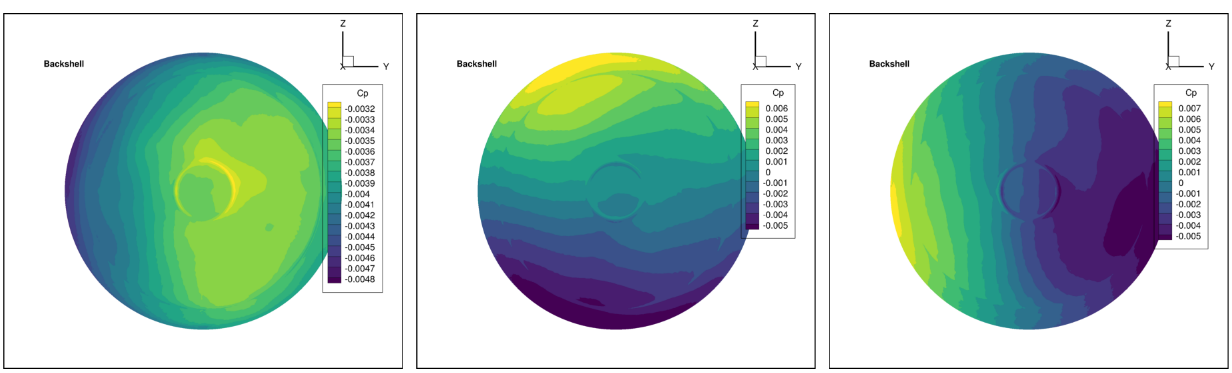

(a) Mode 1 (b) Mode 2 (c) Mode 3

Fig. 6 First 3 POD Modes for Backshell ROM

Figure 7 shows the first three latent coordinates for the heatshield ROM. Latent coordinates are generated by the dot product of the POD modes and the input snapshot matrix. Latent coordinates are organized in the order of maximum information content stored; therefore, latent coordinate 1 contains the most energy of the system, and the subsequent latent coordinates contribute less energy. The first three latent coordinates display noticeable functional behaviors, a strong indicator a regression can be fit successfully to these coordinates.

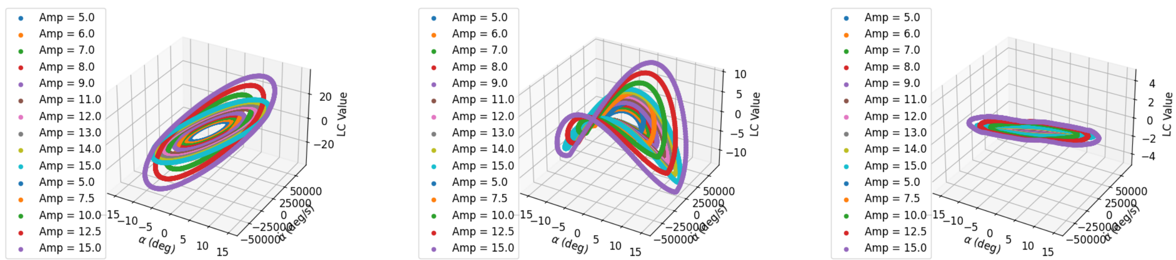

(a) Latent Coordinate 1 (b) Latent Coordinate 2 (c) Latent Coordinate 3

Fig. 7 First 3 Latent Coordinates for Heatshield ROM

Figure 8 shows the first three latent coordinates for the backshell ROM. The backshell latent coordinates display a more chaotic response in all of the latent coordinates, compared to the functional response seen in the first three heatshield latent coordinates. This is a direct result of the nature of vortex shedding and subsonic recirculation occurring on the backshell. The chaotic behavior of the backshell latent coordinates will impact the regression stage of the ROM and the ability to predict unseen latent coordinate values. The characteristics displayed in the latent space of the heatshield and backshell align with literature about the chaotic aerodynamic interactions on entry capsules. In supersonic flow, the bow shock at the front of the vehicle streamlines flow along the heatshield [7], making it easy to isolate the oscillation the vehicle in the latent space. On the backshell, a low pressure region forms behind the shoulder generating a recirculation region [7], resulting in a more chaotic response being picked up by the latent coordinates.

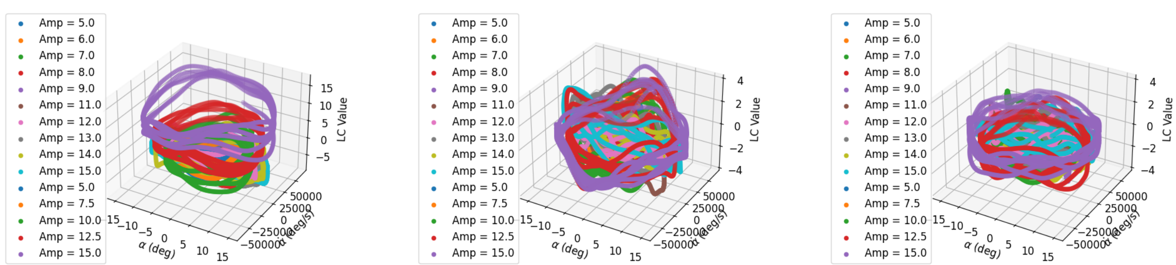

(a) Latent Coordinate 1 (b) Latent Coordinate 2 (c) Latent Coordinate 3

Fig. 8 First 3 Latent Coordinates for Backshell ROM

A Kriging regression was applied to the ROM to predict the unseen motion of a forced oscillation trajectory where $A = 10°$, $f^* = 343.11Hz$, resulting in 1,500 $[\alpha\ \dot{\alpha}]$ pairings to predict the full trajectory. The previously calculated POD modes were applied to the CFD-generated pressure field data from FUN3D, generating the actual latent space of the unseen motion. The Kriging regression was used to predict the unseen latent coordinates at each $[\alpha\ \dot{\alpha}]$ pair. Figure 9 shows the predicted vs actual plots of the first three latent coordinates of the heatshield ROM. As was hypothesized, the Kriging regression could more easily recover the functional form of the first three latent coordinates. The MAE of the regression is calculated using Equation 10. For the heatshield, the MAE is ± 0.2031 latent coordinate units. Given the scale of the latent coordinates shown in Figure 9, this value is well within acceptable bounds. This MAE is summarized in Table 3.

Figure 10 shows the predicted vs actual plots of the first three latent coordinates of the backshell ROM. The Kriging

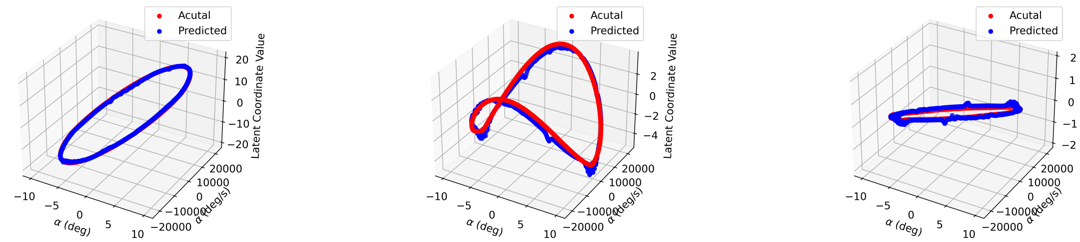

(a) Latent Coordinate 1 (b) Latent Coordinate 2 (c) Latent Coordinate 3

Fig. 9 Predicted vs Actual of First 3 Latent Coordinates for Heatshield ROM

regression has a much harder time predicting the chaotic response of the backshell latent coordinates. This will impact the ability to reconstruct an accurate pressure field using the backshell ROM. The MAE of the regression is calculated using Equation 10. For the backshell, the MAE is ±0.1913 latent coordinate units. Given the magnitude of the backshell latent coordinates shown in Figure 10, this MAE is more significant indicating a poor prediction by the Kriging regression on the backshell. This MAE is summarized in Table 3.

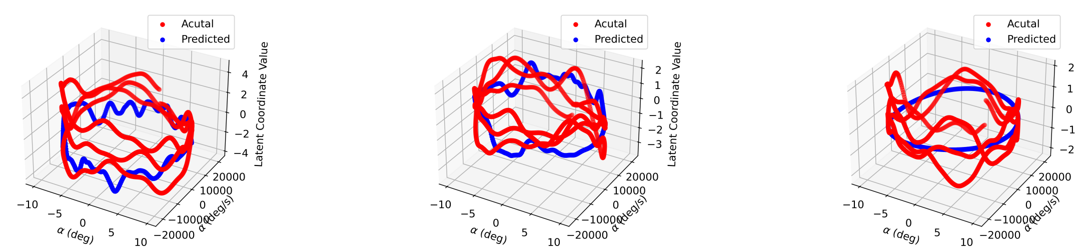

(a) Latent Coordinate 1 (b) Latent Coordinate 2 (c) Latent Coordinate 3

Fig. 10 Predicted vs Actual of First 3 Latent Coordinates for Backshell ROM

Using linear transformations, the FOM can be reconstructed from the predicted latent coordinates. For each $[\alpha, \dot{\alpha}]$ pair in the 1,500 steps that make up the full trajectory, a pressure distribution is reconstructed. A percent difference between the predicted pressure field and actual pressure field at each step is calculated, and then every step is averaged together to condense the ROM accuracy into a single plot. Figure 11 shows the resulting percent difference of the heatshield and backshell ROMs across all 1,500 snapshots in the predicted trajectory. Figure 11(a) shows that the percent difference between the actual and predicted heatshield pressure fields is around 0-10%. The largest errors appear at the shoulder of the vehicle. These discrepancies could be the result of complex aerodynamic interactions like expansion waves that the ROM has challenges accurately predicting. The difference in the shoulder region could be a result of the loss of fidelity as a result of DR, causing the low frequency modes contributing to the results of this region to be discarded. It is also possible that the CFD grid leveraged in this research needs further refinement in the shoulder region to improve the predictive capabilities of the ROM at the shoulder. The MAE of the total field was calculated using Equation 8, with the mean of the heatshield field equal to 0.7539 and the MAE at each node equal to ±0.0034. This is summarized in Table 3.

Figure 11(b) shows much larger discrepancies in the percent difference between the predicted vs actual pressure distributions on the backshell. The percent difference range is lower than on the heatshield; however, there is more significant regions of inaccuracies on the backshell. The first three latent coordinate predictions for the backshell (shown in Figure 10) showed that the predicted latent coordinates are much different then the actual latent coordinates. Therefore, the resulting predicted pressure fields will be different from the actual pressure fields. The mean of the total backshell field is equal to −0.2952, with the MAE at each node equal to ±0.0103. This is summarized in Table 3.

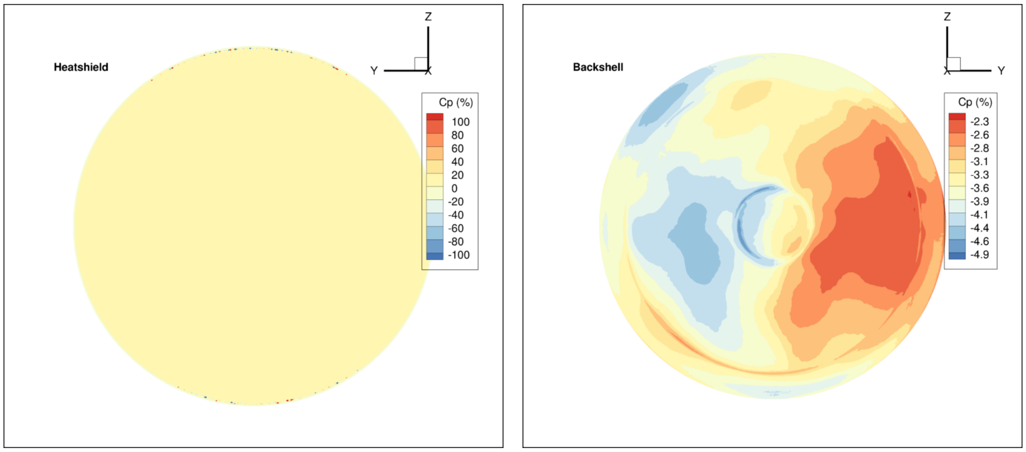

(a) Heatshield

(b) Backshell

Fig. 11 Average Percent Difference Across 1,500 snapshots

Table 3 MAE Summary

Component	Compression Error	Interpolation Error	Total Error
Heatshield	0.7535 ± 0.0018	0.0 ± 0.2031	0.7539 ± 0.0034
Backshell	−0.3064 ± 0.0012	0.0 ± 0.1913	−0.2952 ± 0.0103

The predicted pressure field from the ROM can be integrated into resulting aerodynamic coefficients to explore the accuracy of the predictive capabilities of the ROM. Additionally, it is critical that the ROM is capable of parametric and time-varying prediction of aerodynamic coefficients to explore the dynamic response of the vehicle. Figure 12 shows the aerodynamic coefficient in the x-direction across the sampled trajectory. Figure 12(a) indicates that the this aerodynamic coefficient can be accurately predicted for the heatshield across a validation trajectory, with subtle discrepancies occurring at the peaks of the oscillation cycle. This is likely a result of discrepancies occurring in the predicted latent space, specifically in the second latent coordinate where the predicted field around $\dot{\alpha} = 0$ is noticeably different than the actual latent coordinates (see Figure 9(b)). As expected, challenges in predicting the latent space of the backshell propagate through the predicted pressure field, resulting in discrepancies in the predicted C_{F_x} values across the sampled trajectory for the backshell (shown in Figure 12(b)). However, the resulting aerodynamic coefficients on the backshell are of a similar magnitude, indicating the ROM is doing a decent job in its predictions.

Figure 13 shows the aerodynamic coefficient in the z-direction across the sampled trajectory. As was seen with C_{F_x}, the heatshield coefficient (Figure 13(a)) was accurately predicted across the validation trajectory, with slight differences occurring at peak oscillation amplitudes. The backshell coefficient (Figure 13(b)) was harder to accurately predict; however, the magnitude of the response is still captured by the ROM.

Figure 14 shows the actual vs predicted aerodynamic moment coefficient in the y-direction for the heatshield and backshell. Similar trends can be seen in C_{M_y}, where the heatshield coefficients line up almost exactly, and the backshell coefficients are of the same magnitude, but do not align as precisely as the heatshield. Only C_{F_x}, C_{F_z}, and C_{M_y} are explored in this research because the data set was produced from purely pitching motion. The other resulting aerodynamic coefficients display noisy behavior at significantly small magnitudes.

VI. Conclusion

The results of this research showed promise in using a POD ROM to quantify the dynamic aerodynamics of blunt-body entry vehicles. POD leveraging streaming SVD increased computationally efficiency by reducing the large input snapshot matrices of the heatshield and backshell into usable data. Kriging regression was used to predict unseen latent coordinates, accurately predicting heatshield surface pressure distributions, but having more challenges predicting backshell surface pressure distributions. The ROM was capable of accurately predicting pressure distributions on the

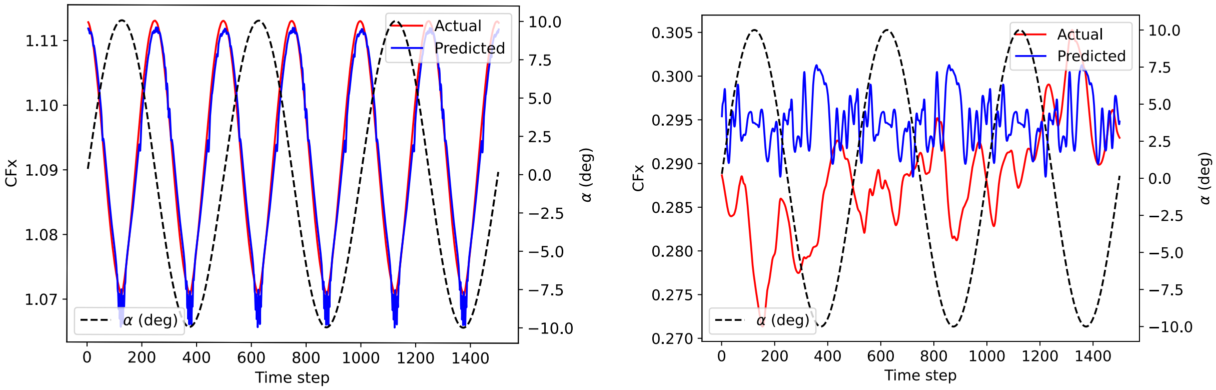

(a) Heatshield (b) Backshell

Fig. 12 Actual vs Predicted C_{F_x} Across the Validation Trajectory

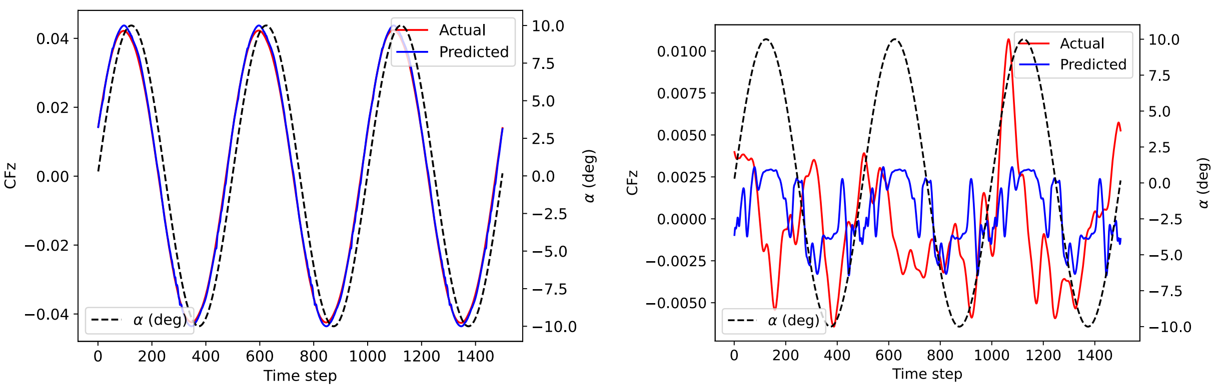

(a) Heatshield (b) Backshell

Fig. 13 Actual vs Predicted C_{F_z} Across the Validation Trajectory

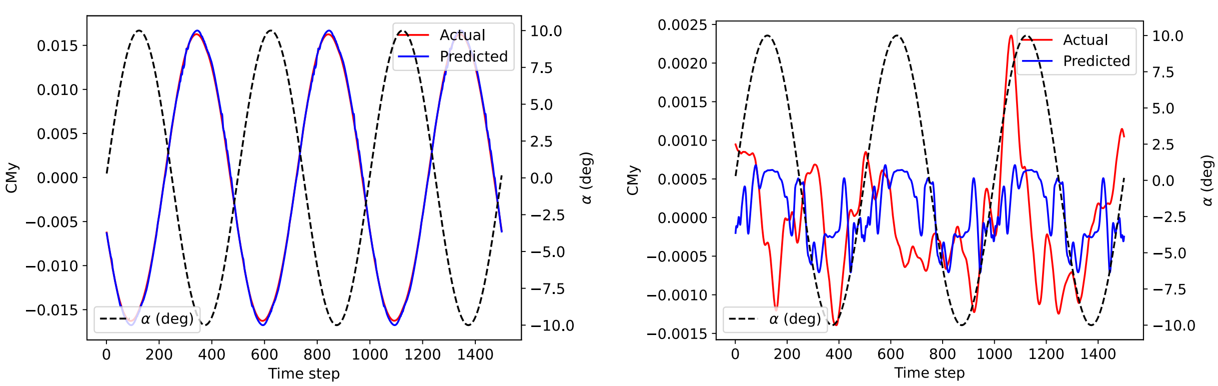

(a) Heatshield (b) Backshell

Fig. 14 Actual vs Predicted C_{M_y} Across the Validation Trajectory

heatshield for unsampled trajectories. The predicted pressure distributions on the backshell were less accurate, but the magnitude of the aerodynamic response was captured. While the focus of this work was to predict the dynamic response of an entry capsule, this methodology can also provide insight into the root cause of dynamic instabilities of entry capsules. The latent space identified in DR isolated chaotic trends in the backshell data set, emphasizing the unsteadiness that contributes to the dynamic response of the vehicle. Additionally, while it is important to note that POD modes are data driven and can sometimes represent non-physical phenomena, the POD modes could indicate surface pressure field characteristics that are driving dynamic instabilities of blunt-body entry vehicles. The extracted POD modes isolate high energy dimensions in the original data field, which might isolate dominate features leading to dynamic instabilities, particularly on the backshell of the entry vehicle.

This research has many avenues of future work to improve and advance these capabilities. The first step is improving the regression stage of the ROM. A Kriging regression has known computational limits, with the computational expense scaling with $O(m^3)$ [56]. While a Kriging regression was implemented on this large data set, the amount of training points is only expected to increase, increasing the burden on the regression. There is literature available that attempts to approximate and scale Gaussian-process regressions [60–62], which can be implemented and leveraged in this problem. Due to the chaotic nature of the backshell latent space, it is possible that additional information (e.g. flow field information, input space parameters, sampled trajectories, higher RIC) would help improve the predictions. All these avenues are being explored in future research. Additionally, this work was constructed on forced oscillation data, which can produce an unrealistic vehicle behavior because the vehicle is being "forced" to move in a sinusoid behavior. Future work in this research will apply this methodology to free-flight CFD data, progressing this methodology to represent more physically consistent entry capsule behavior.

Acknowledgments

This work was supported by an Early Stage Innovations grant 80NSSC23K0229 from NASA's Space Technology Research Grants Program. This project was also supported in part by the Partnership for an Advanced Computing Environment at the Georgia Institute of Technology, who provided computing resources and technical support. This paper was made possible by the data generated from CFD simulations conducted by Brenton Willier, and the grid studies conducted by Alexandra Hickey, both at the Aerospace Systems Design Laboratory at the Georgia Institute of Technology. The authors would also like to thank Eli Shellabarger, Zachary Ernst, and Christian Perron for their support of this work.

References

[1] Schoenenberger, M., and Queen, E., "Limit Cycle Analysis Applied to the Oscillations of Decelerating Blunt-Body Entry Vehicles," 2006.

[2] Edquist, K. T., Desai, P. N., and Schoenenberger, M., "Aerodynamics for Mars Phoenix Entry Capsule," *Journal of Spacecraft and Rockets*, Vol. 48, No. 5, 2011, pp. 713–726. https://doi.org/10.2514/1.46219.

[3] Ericsson, L. E., and Peter Reding, J., "Re-entry Capsule Dynamics," *Journal of Spacecraft and Rockets*, Vol. 8, No. 6, 1971, pp. 579–586. https://doi.org/10.2514/3.59696.

[4] Teramoto, S., Hiraki, K., and Fujii, K., "Numerical analysis of dynamic stability of a reentry capsule at transonic speeds," *AIAA Journal*, Vol. 39, No. 4, 2001, pp. 646–653. https://doi.org/10.2514/2.1357.

[5] Schoenenberger, M., "Supersonic Pitch Damping Predictions of Blunt Entry Vehicles from Static CFD Solutions," *51st AIAA Aerospace Sciences Meeting including the New Horizons Forum and Aerospace Exposition 2013*, , No. January, 2013. https://doi.org/10.2514/6.2013-356.

[6] Schoenenberger, M., Van Norman, J., Rhode, M., and Paulson, J., "Characterization of Aerodynamic Interactions with the Mars Science Laboratory Reaction Control System using Computation and Experiment," *51st AIAA Aerospace Sciences Meeting including the New Horizons Forum and Aerospace Exposition 2013*, , No. January, 2013. https://doi.org/10.2514/6.2013-971.

[7] Kazemba, C. D., Braun, R. D., Clark, I. G., and Schoenenberger, M., "Survey of Blunt-Body Supersonic Dynamic Stability," *Journal of Spacecraft and Rockets*, Vol. 54, No. 1, 2017, pp. 109–127. https://doi.org/10.2514/1.A33552.

[8] Bruce Owens, D., and Aubuchon, V. V., "Overview of Orion Crew Module and Launch Abort Vehicle Dynamic Stability," *29th AIAA Applied Aerodynamics Conference 2011*, , No. June, 2011, pp. 1–24. https://doi.org/10.2514/6.2011-3504.

[9] Moseley Jr, W. C., Moore Jr, R. H., and Hughes, J. E., "Stability Characteristics of the Apollo Command Module," Tech. Rep. March, Manned Spacecraft Center, Houston, TX, 3 1967.

[10] Chapman, G. T., and Yates, L. A., "Limit Cycle Analysis of Planetary Probes," *37th Aerospace Sciences Meeting and Exhibit*, , No. c, 1999. https://doi.org/10.2514/6.1999-1022.

[11] Hickey, A. M., Ernst, Z., Robertson, B. E., and Mavris, D. N., "Demonstration of a coupled CFD-RBD-FCS framework on Mars Science Laboratory Vehicle," *AIAA SCITECH 2023 Forum*, American Institute of Aeronautics and Astronautics, Reston, Virginia, 2023, pp. 359–497. https://doi.org/10.2514/6.2023-1167, URL https://arc.aiaa.org/doi/10.2514/6.2023-1167.

[12] Slotnick, J., Khodadoust, A., Alonso, J., and Darmofal, D., "CFD Vision 2030 Study: A Path to Revolutionary Computational Aerosciences," Tech. Rep. March, NASA, 3 2014.

[13] Ernst, Z., Robertson, B. E., and Mavris, D. N., "Construction of Entry Vehicle Aerodynamic Surrogates from CFD-in-the-loop Flight Simulations," *AIAA SCITECH 2023 Forum*, American Institute of Aeronautics and Astronautics, Reston, Virginia, 2023, pp. 1–19. https://doi.org/10.2514/6.2023-1166, URL https://arc.aiaa.org/doi/10.2514/6.2023-1166.

[14] Murman, S. M., and Aftosmis, M. J., "Dynamic Analysis of Atmospheric-Entry Probes and Capsules," *45th AIAA Aerospace Sciences Meeting*, Vol. 2, 2007. https://doi.org/10.2514/6.2007-74.

[15] Murman, S. M., "Dynamic Viscous Simulations of Atmospheric-Entry Capsules," *AIAA Applied Aerodynamics Conference*, 2008. https://doi.org/10.2514/6.2008-6911.

[16] Stern, E. C., Gidzak, V. M., and Candler, G. V., "Estimation of Dynamic Stability Coefficients for Aerodynamic Decelerators Using CFD," *30th AIAA Applied Aerodynamics Conference 2012*, , No. June, 2012, pp. 2217–2230. https://doi.org/10.2514/6.2012-3225.

[17] Brock, J. M., and Kazemba, C. D., "Dynamic Stability Methodologies and Capabilities," *AIAA SCITECH 2023 Forum*, American Institute of Aeronautics and Astronautics, Reston, Virginia, 2023. https://doi.org/10.2514/6.2023-1335, URL https://arc.aiaa.org/doi/10.2514/6.2023-1335.

[18] McKown, Q. E., Kazemba, C. D., Stern, E. C., and Brock, J. M., "Attitude Reconstruction of Free-Flight CFD Generated Trajectories Using Non-Linear Pitch Damping Coefficient Curve," *AIAA Science and Technology Forum and Exposition, AIAA SciTech Forum 2022*, 2022, pp. 1–18. https://doi.org/10.2514/6.2022-1169.

[19] Decker, K., Iyengar, N., Perron, C., Rajaram, D., and Mavris, D., "Nonlinear Multi-Fidelity Reduced Order Modeling Method using Manifold Alignment," *AIAA Aviation and Aeronautics Forum and Exposition, AIAA AVIATION Forum 2021*, 2021, pp. 1–25. https://doi.org/10.2514/6.2021-3050.

[20] Bui-Thanh, T., Damodaran, M., and Willcox, K., "Proper Orthogonal Decomposition Extensions for Parametric Applications in Compressible Aerodynamics," *21st AIAA Applied Aerodynamics Conference*, , No. June, 2003, pp. 1–11. https://doi.org/10.2514/6.2003-4213.

[21] Rajaram, D., Gautier, R., Perron, C., Fischer, O. J., and Mavris, D. N., "Non-intrusive Parametric Reduced Order Models with High-Dimensional Inputs via Gradient-Free Active Subspace," *Aiaa Aviation 2020 Forum*, Vol. 1 PartF, 2020, pp. 1–30. https://doi.org/10.2514/6.2020-3184.

[22] Rajaram, D., Perron, C., Puranik, T. G., and Mavris, D. N., "Randomized Algorithms for Non-Intrusive Parametric Reduced Order Modeling," *AIAA Journal*, Vol. 58, No. 12, 2020, pp. 5389–5407. https://doi.org/10.2514/1.J059616.

[23] Decker, K. H., Schwartz, H. D., and Mavris, D. N., "Dimensionality Reduction Techniques Applied to the Design of Hypersonic Aerial Systems," *Aiaa Aviation 2020 Forum*, Vol. 1 PartF, 2020, pp. 1–24. https://doi.org/10.2514/6.2020-3003.

[24] Mignolet, M. P., Przekop, A., Rizzi, S. A., and Spottswood, S. M., "A review of indirect/non-intrusive reduced order modeling of nonlinear geometric structures," *Journal of Sound and Vibration*, Vol. 332, No. 10, 2013, pp. 2437–2460. https://doi.org/10.1016/j.jsv.2012.10.017, URL http://dx.doi.org/10.1016/j.jsv.2012.10.017.

[25] Perron, C., Rajaram, D., and Mavris, D. N., "Multi-fidelity non-intrusive reduced-order modelling based on manifold alignment," *Proceedings of the Royal Society A: Mathematical, Physical and Engineering Sciences*, Vol. 477, No. 2253, 2021. https://doi.org/10.1098/rspa.2021.0495.

[26] Iyengar, N., Rajaram, D., Decker, K., Perron, C., and Mavris, D., "Nonlinear Reduced Order Modeling using Domain Decomposition," *AIAA Science and Technology Forum and Exposition, AIAA SciTech Forum 2022*, American Institute of Aeronautics and Astronautics Inc, AIAA, 2022. https://doi.org/10.2514/6.2022-1250.

[27] Benner, P., Gugercin, S., and Willcox, K., "A Survey of Projection-Based Model Reduction Methods for Parametric Dynamical Systems," *SIAM Review*, Vol. 57, No. 4, 2015, pp. 483–531. https://doi.org/10.1137/130932715.

[28] Kerschen, G., Golinval, J. C., Vakakis, A. F., and Bergman, L. A., "The Method of Proper Orthogonal Decomposition for Dynamical Characterization and Order Reduction of Mechanical Systems: An Overview," *Nonlinear Dynamics*, Vol. 41, No. 1-3, 2005, pp. 147–169. https://doi.org/10.1007/s11071-005-2803-2.

[29] Blonigan, P. J., Carlberg, K. T., Rizzi, F., Howard, M., and Fike, J. A., "Model reduction for hypersonic aerodynamics via conservative lspg projection and hyper-reduction," *AIAA Scitech 2020 Forum*, , No. January, 2020, pp. 1–24. https://doi.org/10.2514/6.2020-0104.

[30] Lucia, D. J., and Beran, P. S., "Projection methods for reduced order models of compressible flows," *Journal of Computational Physics*, Vol. 188, No. 1, 2003, pp. 252–280. https://doi.org/10.1016/S0021-9991(03)00166-9.

[31] Iyengar, N., Rajaram, D., Decker, K., and Mavris, D. N., "Uncertainty Propagation in High-Dimensional Fields using Non-Intrusive Reduced Order Modeling and Polynomial Chaos," American Institute of Aeronautics and Astronautics (AIAA), 2023. https://doi.org/10.2514/6.2023-1686.

[32] Xiao, D., Fang, F., Pain, C. C., and Navon, I. M., "A parameterized non-intrusive reduced order model and error analysis for general time-dependent nonlinear partial differential equations and its applications," *Computer Methods in Applied Mechanics and Engineering*, Vol. 317, 2017, pp. 868–889. https://doi.org/10.1016/j.cma.2016.12.033.

[33] Dol, S. S., "Proper orthogonal decomposition analysis of vortex shedding behind a rotating circular cylinder," *EPJ Web of Conferences*, Vol. 114, 2016, pp. 1–8. https://doi.org/10.1051/epjconf/201611402019.

[34] Berkooz, G., Holmes, P., and Lumley, J. L., "The Proper Orthogonal, Decomposition in the Analysis of Turbulent Flows," 1993. https://doi.org/10.1146/annurev.fluid.25.1.539.

[35] Johansson, P. B., George, W. K., and Woodward, S. H., "Proper orthogonal decomposition of an axisymmetric turbulent wake behind a disk," *Physics of Fluids*, Vol. 14, No. 7, 2002, pp. 2508–2514. https://doi.org/10.1063/1.1476301.

[36] Bui-Thanh, T., Willcox, K., and Ghattas, O., "Parametric Reduced-Order Models for Probabilistic Analysis of Unsteady Aerodynamic Applications," *AIAA Journal*, Vol. 46, No. 10, 2008, pp. 2520–2529. https://doi.org/10.2514/1.35850.

[37] Swischuk, R., Mainini, L., Peherstorfer, B., and Willcox, K., "Projection-based model reduction: Formulations for physics-based machine learning," *Computers and Fluids*, Vol. 179, 2019, pp. 704–717. https://doi.org/10.1016/j.compfluid.2018.07.021.

[38] Chen, W., Junqiang, B., and Hesthaven, J. S., "An iterative approach to improve Non-Intrusive Reduced-Order Models efficiency for parameterized problems," *21st AIAA International Space Planes and Hypersonics Technologies Conference, Hypersonics 2017*, , No. March, 2017. https://doi.org/10.2514/6.2017-2348.

[39] Li, J., and Zhang, W., "The performance of proper orthogonal decomposition in discontinuous flows," *Theoretical and Applied Mechanics Letters*, Vol. 6, No. 5, 2016, pp. 236–243. https://doi.org/10.1016/j.taml.2016.08.008.

[40] Franz, T., Zimmermann, R., Görtz, S., and Karcher, N., "Interpolation-based reduced-order modelling for steady transonic flows via manifold learning," *International Journal of Computational Fluid Dynamics*, Vol. 28, No. 3-4, 2014, pp. 106–121. https://doi.org/10.1080/10618562.2014.918695.

[41] Fossati, M., "Evaluation of Aerodynamic Loads via Reduced-Order Methodology," *AIAA Journal*, Vol. 53, No. 8, 2015, pp. 2389–2405. https://doi.org/10.2514/1.J053755.

[42] Barraza, B., Wei, Z., and Gross, A., "Reduced-Order Modeling of Steady and Unsteady Flows with Deep Neural Networks," *AIAA AVIATION 2022 Forum*, 2022, pp. 1–14. https://doi.org/10.2514/6.2022-3978.

[43] Hasegawa, K., Fukami, K., Murata, T., and Fukagata, K., "CNN-LSTM based reduced order modeling of two-dimensional unsteady flows around a circular cylinder at different Reynolds numbers," *Fluid Dynamics Research*, Vol. 52, IOP Publishing Ltd, 2020. https://doi.org/10.1088/1873-7005/abb91d.

[44] Noack, B. R., Stankiewicz, W., Morzyński, M., and Schmid, P. J., "Recursive dynamic mode decomposition of transient and post-transient wake flows," *Journal of Fluid Mechanics*, Vol. 809, 2016, pp. 843–872. https://doi.org/10.1017/jfm.2016.678.

[45] Amsallem, D., and Farhat, C., "Interpolation method for adapting reduced-order models and application to aeroelasticity," *AIAA Journal*, Vol. 46, No. 7, 2008, pp. 1803–1813. https://doi.org/10.2514/1.35374.

[46] Andersen, S. J., and Murcia Leon, J. P., "Predictive and stochastic reduced-order modeling of wind turbine wake dynamics," *Wind Energy Science*, Vol. 7, No. 5, 2022, pp. 2117–2133. https://doi.org/10.5194/wes-7-2117-2022.

[47] Bastine, D., Vollmer, L., Wächter, M., and Peinke, J., "Stochastic wake modelling based on POD analysis," *Energies*, Vol. 11, No. 3, 2018. https://doi.org/10.3390/en11030612.

[48] Taira, K., Brunton, S. L., Dawson, S. T., Rowley, C. W., Colonius, T., McKeon, B. J., Schmidt, O. T., Gordeyev, S., Theofilis, V., and Ukeiley, L. S., "Modal Analysis of Fluid Flows: An Overview," *AIAA Journal*, Vol. 55, No. 12, 2017, pp. 4013–4041. https://doi.org/10.2514/1.J056060.

[49] Taira, K., Hemati, M. S., Brunton, S. L., Sun, Y., Duraisamy, K., Bagheri, S., Dawson, S. T., and Yeh, C. A., "Modal Analysis of Fluid Flows: Applications and Outlook," *AIAA Journal*, Vol. 58, No. 3, 2020, pp. 998–1022. https://doi.org/10.2514/1.J058462.

[50] Owens, B., Brandon, J., Croom, M., Fremaux, M., Heim, G., and Vicroy, D., "Overview of Dynamic Test Techniques for Flight Dynamics Research at NASA LaRC," American Institute of Aeronautics and Astronautics (AIAA), 2006. https://doi.org/10.2514/6.2006-3146.

[51] Anderson, W. K., Biedron, R. T., Carlson, J.-R., Derlaga, J. M., Druyor, C. T., Gnoffo, P. A., Hammond, D. P., Jacobson, K. E., Jones, W. T., Kleb, B., Lee-Rausch, E. M., Nastac, G. C., Nielsen, E. J., Park, M. A., Rumsey, C. L., Thomas, J. L., Thompson, K. B., Walden, A. C., Wang, L., Wood, S. L., Wood, W. A., Diskin, B., Liu, Y., and Zhang, X., "FUN3D Manual: 14.0.1," Tech. rep., 2023. URL http://www.sti.nasa.gov.

[52] Tropea, C., Yarin, A., and Foss, J., *Springer Handbook of Experimental Fluid Mechanics*, 2007.

[53] Maulik, R., and Mengaldo, G., "PyParSVD: A streaming, distributed and randomized singular-value-decomposition library," *Proceedings of DRBSD-7 2021: 7th International Workshop on Data Analysis and Reduction for Big Scientific Data, Held in conjunction with SC 2021: The International Conference for High Performance Computing, Networking, Storage and Analysis*, Institute of Electrical and Electronics Engineers Inc., 2021, pp. 19–25. https://doi.org/10.1109/DRBSD754563.2021.00007.

[54] Levy, A., and Lindenbaum, M., "Sequential Karhunen-Loeve Basis Extraction and its Application to Images," *IEEE Transactions on Image Processing*, Vol. 9, No. 8, 2000.

[55] Aversano, G., D'Alessio, G., Coussement, A., Contino, F., and Parente, A., "Combination of polynomial chaos and Kriging for reduced-order model of reacting flow applications," *Results in Engineering*, Vol. 10, 2021. https://doi.org/10.1016/j.rineng.2021.100223.

[56] Rasmussen, C. E., and Williams, C. K. I., *Gaussian Processes for Machine Learning*, The MIT Press, 2005. https://doi.org/10.7551/mitpress/3206.001.0001.

[57] Cheatwood, F., Winchenbach, G. L., Hathaway, W., and Chapman, G., "Dynamic Stability Testing of the Genesis Sample Return Capsule," *38th Aerospace Sciences Meeting and Exhibit*, , No. c, 2000. https://doi.org/10.2514/6.2000-1009.

[58] Desai, P. N., and Cheatwood, F. M., "Entry Dispersion Analysis for the Genesis Sample Return Capsule," *Journal of Spacecraft and Rockets*, Vol. 38, No. 3, 2001, pp. 345–350. https://doi.org/10.2514/2.3707.

[59] Willier, B. J., Hickey, A. M., Robertson, B. E., and Mavris, D. N., "Unsteady Aerodynamic Uncertainty Quantification of a Blunt-Body Entry Vehicle in Free-Flight," *AIAA SCITECH 2024 Forum*, 2024.

[60] Titsias, M. K., "Variational Learning of Inducing Variables in Sparse Gaussian Processes," Tech. rep., 2009.

[61] Quiñonero, J., Quiñonero-Candela, Q., Rasmussen, C. E., and De, C. M., "A Unifying View of Sparse Approximate Gaussian Process Regression," Tech. rep., 2005.

[62] Wilson, A. G., Dann, C., and Nickisch, H., "Thoughts on Massively Scalable Gaussian Processes," 2015. URL http://arxiv.org/abs/1511.01870.